

NICMOS 2 MICRON CONTINUUM AND H₂ IMAGES OF OMC-1

SUSAN R. STOLOGY,¹ MICHAEL G. BURTON,² EDWIN F. ERICKSON,³ MICHAEL J. KAUFMAN,^{3,4} ANTONIO CHRYSOSTOMOU,^{5,6}
 ERICK T. YOUNG,¹ SEAN W. J. COLGAN,^{3,7} D. J. AXON,⁸ RODGER I. THOMPSON,¹
 MARCIA J. RIEKE,¹ AND GLENN SCHNEIDER¹

Received 1997 August 2; accepted 1997 October 30; published 1997 December 30

ABSTRACT

The core of OMC-1 has been imaged with the Near-Infrared Camera and Multiobject Spectrometer (NICMOS) on board the *Hubble Space Telescope* at 0".2 resolution in 1% filters at 2.12 and 2.15 μm , revealing intricate structures in both continuum and shocked molecular hydrogen line emission. Numerous H₂-emitting clumps surrounding the BN/KL region have been resolved for the first time, several of which exhibit prototypical bow-shock morphologies with V-shaped tips. We interpret these to be lower excitation analogs of similar structures ~2' northwest of the core observed with ground-based telescopes. Many of the elongated H₂ structures and bow-shock features appear to radiate outward from a region within a few arcseconds of radio source I, which suggests that the H₂ energetics are dominated by one or more outflow sources in this region. However, the orientations of some features are unrelated to this apparent outflow pattern. The deeply embedded, suspected outflow source I remains undetected at 2 μm , although two faint new continuum sources have been detected within ~1" of it. The newly resolved H₂ features with bow-shock morphologies are located in regions previously identified as bow shocks by highly blueshifted components in their line profiles. In contrast, regions of H₂ emission that are diffuse in the NICMOS image have broad, smooth line profiles. Several continuum features have an arclike appearance, which suggests interactions of winds with the ambient medium. At least 40 stellar or protostellar continuum sources have been detected, including at least one proplyd and four pairs of binary stars.

Subject headings: binaries: close — infrared: ISM: continuum — ISM: individual (OMC-1) — ISM: jets and outflows — ISM: molecules — shock waves

1. INTRODUCTION

OMC-1 was the first astronomical object in which H₂ emission was detected (Gautier et al. 1976; Beckwith et al. 1978). The 2.12 μm $v = 1 \rightarrow 0$ S(1) H₂ emission is known to be shock excited from thermal line ratios (Beckwith et al. 1978) and broad line profiles (Nadeau & Geballe 1979) and is thought to arise from shocks formed when outflowing gas from one or more young stellar objects interacts with the ambient molecular cloud. The dramatic outflows in the vicinity of the Becklin-Neugebauer object/Kleinmann-Low nebula (BN/KL) challenge our understanding of shock physics with each advance in spectral and spatial resolution (see, e.g., Burton 1992; Brand 1995). The Near-Infrared Camera and Multiobject Spectrometer (NICMOS) (Thompson et al. 1997) has allowed us to study the 2.12 μm H₂ line and continuum structures of OMC-1 in greater detail than ever before.

2. OBSERVATIONS

These data were obtained during five consecutive orbits of the *Hubble Space Telescope* (HST) on 1997 April 12 and 13,

during the check-out phase of the newly installed NICMOS. Diffraction-limited images were obtained with camera 2 through two 1% filters with central wavelengths of 2.121 μm (F212N) and 2.149 μm (F215N). Each orbit consisted of seven 160 s exposures with F212N followed by a similar sequence with F215N. A large dynamic range was achieved by reading out the array nondestructively 13 times during each exposure. The telescope pointing was changed for each of the five orbits but remained fixed during a single orbit. The five orbits had different orientations, ranging from $-118^\circ 33'$ to $-122^\circ 62'$ (position angle of y-axis east of north). Very faint "electronic ghosts" appear 128 pixels away from saturated pixels because of electrical crosstalk between quadrants. The plate scale, determined on April 17 by the Space Telescope Science Institute (STScI), was $0''.076320 \text{ pixel}^{-1}$ in x and $0''.075655 \text{ pixel}^{-1}$ in y (both values $\pm 0''.000028 \text{ pixel}^{-1}$).

3. DATA REDUCTION AND ANALYSIS

The initial data reduction was done with a customized version of the CALNICA software developed by STScI to reduce NICMOS images. Direct current levels were first removed by subtracting an initial "zeroth read" exposure. A previously determined mask excluded bad pixels from further processing. The dark current was subtracted with a matching readout sequence of exposures taken with the blank filter. Each pixel in the array was linearized with a fit to unsaturated exposures. The images were flat-fielded with an internal NICMOS flat lamp for each filter. A weighted linear fit to the counts in each readout sequence was done for each pixel. The weighting accounted for accumulated uncertainties and excluded readouts where cosmic rays were detected. Finally, the seven exposures were averaged, giving a total integration time of 18.7 minutes for each of the five positions in each filter.

¹ Steward Observatory, University of Arizona, Tucson, AZ 85721; sstology@as.arizona.edu.

² School of Physics, University of New South Wales, Sydney, NSW 2052, Australia.

³ NASA Ames Research Center, Space Science Division, Moffett Field, CA 94035-1000.

⁴ Department of Astronomy, University of California, Berkeley, Berkeley, CA 94720.

⁵ Joint Astronomy Centre, 660 North A'ohoku Place, Hilo, HI 96720.

⁶ On leave from the Department of Physical Sciences, University of Hertfordshire, Hatfield, AL10 9AB, England, UK.

⁷ Search for Extraterrestrial Intelligence Institute.

⁸ Astrophysics Division of ESA, Space Telescope Science Institute, 3700 San Martin Drive, Baltimore, MD 21218.

Mosaics of the inner arcminute of OMC-1 were constructed for each filter, resulting in maps covering an area of ~ 0.1 pc centered near BN. The 256×256 pixel images were rebinned to 516×511 images to correct the nonsquare aspect ratio and to allow for a more accurate registration of spatially overlapping images. Each image was rotated so that north was up and east was to the left. A cubic spline interpolation was used for all rebinning and rotation procedures. The pixels corresponding to the coronagraphic hole (always present in camera 2 images) were replaced by good overlapping pixels where possible and were set to zero for nonoverlapping regions. Bad pixels were replaced by overlapping good pixels or by a median of neighboring pixels, and each pixel was weighted by its integration time. Overlapping images were registered by aligning stars and bright, diffuse features. The F212N and F215N mosaics were produced with identical rotations and offsets. The resulting alignment accuracy is $\approx 0''.02$ (half of the small pixel size). Finally, the pixels were binned by a factor of 2 to approximate the size of original detector pixels, producing square pixels with a plate scale of $0''.07577$ pixel $^{-1}$. The effects on point-spread functions due to rotation and rebinning caused a minimal amount of broadening (less than 3% FWHM). The measured FWHM of bright point sources of $2.4 (\pm 0.1)$ pixels ($0''.18$) corresponds to 84 AU, or 1.2×10^{15} cm, for an assumed distance to OMC-1 of 450 pc (Genzel & Stutzki 1989).

Each mosaic was flux calibrated on the basis of observations of the solar analog star P330-E as part of the NICMOS calibration program. The relative flux calibration of the F212N and F215N filters is estimated to be correct to 3%. The H_2 line emission image was formed by subtracting the flux-calibrated F215N mosaic from the F212N mosaic. The absolute photometry of the stars compares favorably (to $\pm 20\%$) with ground-based *K*-band photometry (M. J. McCaughrean 1997, private communication). A subpixel mismatch of the centroids of the stars between the two filters was corrected by shifting the F215N mosaic north by 0.20 pixel ($0''.015$). The 1σ noise level in the areas of the mosaics without overlap was $\sim 7 \times 10^{-4}$ mJy pixel $^{-1}$. Figures 1 and 2 (Plates L37 and L38) display the continuum and H_2 line emission mosaics, respectively, with coordinate axes relative to BN. Various continuum features discussed in this work are labeled on Figure 1 for reference. Figure 3 (Plate L39) shows the continuum image overlaid with contours of the H_2 emission.

4. RESULTS AND DISCUSSION

4.1. Molecular Hydrogen Emission

Morphology.—The H_2 line emission from OMC-1 arises from a multitude of clumps distributed over a wide angular range centered on and extending $\sim 30''$ from BN, together with a series of hollow “fingers” pointing predominantly to the northwest (NW) for a further $\sim 60''$. These NW fingers (out of the field of the NICMOS images) are each capped by a higher excitation Herbig-Haro object (see, e.g., Allen & Burton 1993, hereafter AB). The NICMOS data (Fig. 2) now reveal that the clumpy emission around BN contains sharply defined H_2 fingers in addition to a more diffuse component. These H_2 fingers are very similar in both length, $\sim (1-3) \times 10^{16}$ cm, and appearance to those seen to the NW, except that Figure 2 shows the H_2 emission in both the heads (tips) and wakes (fingers) of the bow shocks; in contrast, only the wakes are seen in H_2 in the NW fingers. Substructure is evident on the scale of $\sim 3 \times 10^{15}$ cm. Many of the fingers exhibiting prototypical, V-shaped bow-

shock structures are located southwest (SW) of BN. The H_2 line fluxes for these bow-shock features are a few times 10^{-13} ergs s $^{-1}$ cm $^{-2}$, in $1''.5$ diameter apertures. Other bright fingers are seen to the southeast (SE), and fainter fingers are seen extending to the northeast (NE). Differences in morphologies could be related to the viewing angle of the observer relative to the motions of the shocked gas blobs. The diffuse, clumpy H_2 emission located $\sim 20''$ NW of BN is known from lower resolution images as Peak 1 (see, e.g., Beckwith et al. 1978). A similar region known as Peak 2 is located $\sim 25''$ SE of BN, but only a portion of it is visible at the SE edge of Figure 2. We also note that HH 208, optically identified by its [O I] and [S II] emission and located $\sim 7''$ west of BN, has no H_2 counterpart in the NICMOS image, which indicates that it is a foreground object.

Bow shocks.—Dense knots, or “bullets,” of gas interacting at supersonic speeds with ambient molecular gas will produce bow shocks. Along the bow, from tip to wake, the shock velocity changes as the normal component of the bullet speed, and the excitation will decrease. Emission lines of, for instance, [O III] and $H\alpha$ at the tip have been observed to give way to those of [S II] and [Fe II] and then to H_2 in the wake (see, e.g., AB; O’Dell et al. 1997). Spatially resolved line profiles will also show changing high-velocity components along the wakes of bow shocks. Such a morphology and excitation led AB to identify the NW fingers as bow shocks, driven by the expansion of dense bullets at high speeds and originating from a source at or near IRc2. The NW fingers have been observed to have full width at zero intensity (FWZI) line widths of 100–400 km s $^{-1}$ (Axon & Taylor 1984; Tedds et al. 1995). The largest line widths are from atomic species such as [O I] 6300 Å and [Fe II] 1.64 μ m. Hartigan, Raymond, & Hartmann (1987) showed that the FWZI of the line gives the bullet speed independent of viewing angle. Chrysostomou et al. (1997, hereafter CBA) identified localized but spatially unresolved regions near the core of OMC-1 as additional “bullets” from H_2 line profiles with blueshifted components of up to 150 km s $^{-1}$. The nondetection of [Fe II] in the core (AB) may be partially explained by the lower resolution of the ground-based images (assuming that the [Fe II] is concentrated at the bullet tips) coupled with higher extinction at 1.64 μ m. However, the bullet tips are seen in H_2 , which suggests that the core region is characterized by slower shock speeds than the NW fingers. Higher resolution [Fe II] images from NICMOS will help to confirm this interpretation.

We find no obvious correlation between H_2 clumps and the H_2O masers presented in Genzel et al. (1981). Although the shock models proposed to explain the maser emission from outflow regions are relatively efficient at producing 2.12 μ m H_2 emission (see, e.g., Elitzur, Hollenbach, & McKee 1989; Kaufman & Neufeld 1996), H_2O maser features exhibit typical dynamical lifetimes of only ~ 10 yr (Genzel 1992), so a precise correlation may not be expected. In addition, the expected filling factor of masing gas ($n \geq 10^7$ cm $^{-3}$) is far smaller than that of nonmasing but H_2 -emitting shocked gas ($n \sim 10^5$ cm $^{-3}$).

Comparisons with line profiles.—CBA measured H_2 line profiles with $1''.5$ and 14 km s $^{-1}$ resolution in OMC-1 and identified two characteristic types: broad smooth profiles centered on the 9 km s $^{-1}$ rest velocity of the cloud that pervades the entire region (Scoville et al. 1983) and high-velocity blueshifted components from discrete locations. Remarkably, there is a close correspondence between the regions with high-velocity components (see Fig. 7 of CBA) and the V-shaped bow-shock

features in the NICMOS image. In contrast, the smooth profiles originate from regions that exhibit diffuse and filamentary structure in the NICMOS image. Figure 4 (Plate L40) displays enlargements of three selected regions of the NICMOS H_2 image and their corresponding line profiles from CBA. Diffuse emission from the Peak 1 region $\sim 10''$ W, $18''$ N of BN is shown to have a smooth, symmetric profile. A complex feature with “nested arcs” located $\sim 7''$ W, $9''$ S of BN has a smooth profile with only moderately blueshifted emission. In contrast, the classic bow shock (bullet) $5''$ to its west has a very asymmetric profile, with discrete components blueshifted up to 100 km s^{-1} .

The observation of H_2 with line widths significantly larger than traditionally adopted shock dissociation speeds has long been a puzzle. One model that self-consistently reconciles this problem introduces a strong “shock-absorbing” magnetic field (Smith, Brand, & Moorhouse 1991). If the thickness of the wakes measured in the NICMOS image ($\sim 4 \times 10^{16} \text{ cm}$) corresponds to the cooling length of a C shock, the Alfvén Mach number and hence the magnetic field strength can be constrained (Smith et al. 1991). It would imply field strengths of order 10 mG, comparable to that estimated from imaging polarimetry (Chrysostomou et al. 1994). The knots within the wakes might represent entrainment of material, inhomogeneities in the medium, and/or internal bow shocks.

Possible origins.—A multitude of fingers now observed in OMC-1—including many among those to the NW seen by AB, those discovered $80''$ SE of BN (McCaughrean & MacLow 1997), and those within $20''$ of BN now resolved by NICMOS—point toward a common origin somewhat south of BN. The wakes in Figure 2 that can be traced back to this vicinity, e.g., the ones located $\sim 6''$ E, $14''$ N and $12''$ W, $9''$ S of BN, intersect within a radius of $\sim 4''$ of radio source I, located $5''.89$ E and $7''.64$ S of BN (Menten & Reid 1995, hereafter MR). This intersection region includes source n and excludes BN, but no clearer identification can be made. Radio source I has been identified as the exciting source of SiO masers and is thought to be a luminous ($\geq 10^4 L_\odot$) evolved star possibly also responsible for powering the reradiated luminosity of the IRC2 complex (MR). Source n is coincident with a double-lobed, variable radio source and is close to the center of expansion of high-velocity interstellar water masers; MR suggest that it may be a secondary outflow source, besides I, in the OMC-1 core. The technique of locating outflow sources by tracing back the elongation directions of the fingers assumes that their orientations preserve the history of their passage through the medium and that it occurs in a straight line. We note that there are several V-shaped structures (e.g., to the SE, SW, and NE) that exhibit large deviations from the general radial outflow morphology discussed above. This may be due to deflections of the outflowing material by a clumpy medium and/or the presence of additional outflow sources significantly displaced from I and n. The mechanism that produces the flow morphology as charted by the finger orientations may be tunnels or fissures existing in the density structure of the local medium when the outflow begins (O’Dell et al. 1997).

The locations of the inner bullets $\sim 15''$ from I indicate dynamical timescales of order ~ 200 – 1000 yr , assuming a generous range of expansion velocities of 30 – 150 km s^{-1} . The 1000 yr limit is comparable to the dynamical timescale for the outer (faster) fingers, indicating that both sets of outflows could have resulted from a single, explosive event. The inner fingers could also, however, represent a more recent ejection phase.

We also note that there are some irregular H_2 clumps within only $2''$ – $5''$ of I. It is possible that these clumps are foreshortened structures of common origin with the longer fingers farther from the core but are traveling closer to the line of sight.

As discussed by Stone, Xu, & Mundy (1995), the bullets probably were not produced at the outflow source but possibly condensed in situ as a result of instabilities from the interaction of a wind with an expanding shell. This model predicts that behind the fingers (closer to the outflow source), the shell should break up into clumps. Clumps have been observed behind the outer NW fingers with ground-based telescopes. One intriguing feature in the NICMOS image that may represent such an instability is located $\sim 7''$ W, $9''$ S of BN and appears to contain three “nested arcs” spaced $\sim 0''.3$ ($2 \times 10^{15} \text{ cm}$) apart. This feature is along the projected path between the outflow source and the bullet to its west (see close-up in Fig. 4c). If these features are causally related, they may provide evidence for fragmentation in an interaction region that resulted in the expulsion of the bullet. We caution, however, that this is the only clear instance of a clump/bullet pairing in the NICMOS field. The nested appearance of the eastern feature also may indicate multiple or nonsteady outflows.

4.2. Continuum Emission

Stars.—Approximately 40 stars brighter than $m_K \sim 15.5$ have been detected in the continuum image (taking $m_{2.15} \approx m_K$). Several stars are detected with fluxes between $m_K \sim 15.5$ and 17, but fainter stars are not apparent despite the expected 3σ detection limit of $m_K \sim 19$. Accurate photometry is also limited by the strong, diffuse continuum emission. Only eight stars appear to be in close binary systems, in contrast to the high (50%–60%) companion fraction seen at K band in other star-forming regions (Ghez et al. 1997). These close binaries, labeled CB1–CB4 in order of increasing right ascension in Figure 1, have projected separations ranging from ~ 100 to 250 AU . Two pairs have been identified as binaries from optical *HST* studies; CB1 is also known as PC33/PC34, and CB3 is known as PC59/PC60 (Prosser et al. 1994). Only in CB2 do the stars in the binary differ in brightness significantly (by more than 50%) at $2 \mu\text{m}$. Proplyd 154-240, identified optically by O’Dell et al. (1997), is located $19''.1$ E, $17''.1$ S of BN. It appears as a compact source superposed on faint diffuse emission in the $2 \mu\text{m}$ continuum and has no clear H_2 counterpart. Two faint but extended objects that may also be protostellar in nature are located $8''.6$ E, $2''.5$ N and $8''.1$ E, $15''.9$ S of BN.

BN and immediate surroundings.—BN is by far the brightest object in the NICMOS mosaic, with its diffraction pattern still evident at least $20''$ away from the centroid. It is not, however, the dominant luminosity source in OMC-1; this distinction belongs to IRC2, as discussed below. BN has been modeled as a $10^4 L_\odot$ B0.5 zero-age main-sequence star (Scoville et al. 1983), whose systematic velocity of 12 km s^{-1} with respect to OMC-1 and proper motion relative to source I of $\sim 0''.02 \text{ yr}^{-1}$ suggest that it is an interloper moving through the core of OMC-1 by chance (Plambeck et al. 1995). BN has a relatively high degree of polarization (see, e.g., Hough et al. 1996), which suggests that it is deeply embedded behind the OMC-1 outflow region. The spectral properties of BN suggest that there is a dust shell close to the star (Dougados et al. 1993). The elongated, clumpy cloud extending $\sim 0.03 \text{ pc}$ to the NE of BN in the NICMOS image coincides with the dust ridge seen at far-infrared (FIR) wavelengths (see, e.g., Wright et al. 1992). The

polarimetry of Minchin et al. (1991) suggests that BN is illuminating this NE extension. A distinct feature identified as “I” by Lonsdale et al. (1982) is located $\sim 2''$ E, $3''$ N of BN and is clearly extended in the NICMOS image. The relationship, if any, between I and BN is uncertain. BN departs from a point source even in the first Airy ring (which is “burned out” in the display stretch of Figs. 1 and 3).

IRc2, I, n, and IRc7.—IRc2 is the most luminous source ($2\text{--}10 \times 10^4 L_\odot$) in the OMC-1 core (Genzel & Stutzki 1989). Despite the fact that IRc2 is easily detected at FIR wavelengths, it is virtually invisible at $2 \mu\text{m}$ because of a large line-of-sight extinction. IRc2 has been resolved into four components at $3.8 \mu\text{m}$ (IRc2-A through IRc2-D; Dougados et al. 1993). Figure 5a (Plate L41) reveals a faint ($m_K \sim 16.5$) source that is coincident with IRc2-B, located $5''.7$ E, $6''.6$ S of BN. The other three components have no clear $2 \mu\text{m}$ counterpart (C is under the diffraction spike from n). It is not surprising that radio source I is not detected in the NICMOS image, as it is known to be deeply embedded (see, e.g., Dougados et al. 1993). Another new, faint $2 \mu\text{m}$ source is located $6''.7$ E, $8''.1$ S of BN. The bright star located $12''.0$ E, $16''.4$ S of BN is producing a weak electronic ghost within a pixel of this source. However, the source is real, since it is detected in the overlapping exposures with no bright star 1 quadrant away. Source n, located $3''.6$ E, $9''.9$ S of BN, is pointlike in the NICMOS image. IRc7 is a compact but has a fanlike tail (see Fig. 5a) extending away from source n. The wide angle of this fan and its proximity to n suggest that a wind from n may be forming the tail.

IRc3 and IRc4.—The NICMOS images now reveal that IRc3 and IRc4 are diffuse arcs, bent away from the IRc2/BN region and studded with bright, resolved knots. Their curvature may be shaped by winds from the IRc2 region. On the basis of their near-IR polarization, Minchin et al. (1991) interpret the continuum emission of IRc3, IRc4, and IRc7 as scattered radiation from a source in the vicinity of the IRc2 complex. They are therefore likely to be externally illuminated condensations, as is also implied by the lack of clear stellar signatures along the arcs. The bright ($m_K \sim 10$) star at the southern end of IRc4 is likely a foreground object, as it is seen optically (O’Dell et al. 1997). Another star at the eastern end of IRc3 is reddened, but its relation to IRc3 is unclear.

The Shell.—A faint partial shell structure with a nearly perfectly uniform radius of curvature is seen for the first time (see Fig. 5b). The Shell radius is ~ 1550 AU, with a center of curvature displaced slightly ($\sim 0''.3$) east of the star located $16''.2$ E, $13''.9$ S of BN. Although the Shell is chiefly a continuum feature (scattered light), there is some faint H_2 emission ($\leq 2.0 \times 10^{-16}$ ergs $\text{s}^{-1} \text{cm}^{-2} \text{pixel}^{-1}$) curving along its NE boundary; this could be either shocked by an outflow or ra-

diatively excited by the star. The Shell is not delineated in H_2 emission to the south, where the much stronger fingers in the Peak 2 region dominate. The proplyd 154-240 can also be seen near the SE edge of Figure 5b.

The Crescent.—One of the most fascinating new discoveries from the continuum NICMOS image is the crescent-shaped feature located $\sim 2''$ W, $9''$ N of BN. A close-up view of this feature, which we dub “the Crescent,” is shown in Figure 5c. The Crescent may be illuminated by BN, IRc2, or both. The dark area to the NW of the Crescent appears to be in shadow. The general lack of H_2 emission (see Fig. 3) could imply that the Crescent is not currently being shocked. However, the faint H_2 emission at the NE edge could instead indicate that most of the H_2 has been dissociated, and H_2 emission is seen only where the normal component of an impinging wind from the SE would be small. Two additional diffuse continuum features are seen to the north and west of the Crescent, “downstream” relative to the outflow. Their morphology and spatially symmetric locations behind the Crescent suggest that the Crescent is the illuminated edge of a dense condensation and that these “downstream” features form a wake or may have broken off of the Crescent in response to the outflow from the SE. The Crescent may be an example of a protostellar object in a delicate balance between collapse and disruption. We note that another, fainter feature seen $\sim 11''$ SW of the Crescent (see Fig. 5c) has what appears to be a faint filamentary wake and a dark shadow extending $\sim 2''$ in the direction opposite IRc2/BN.

5. CONCLUSIONS

The NICMOS data reveal a plethora of elongated structures emitting entirely in H_2 in the core of OMC-1, some tipped with well-defined bow-shock morphologies. We interpret these as slower moving analogs of the fingers and bullets previously observed $\sim 2'$ to the NW. Together, they suggest that within the past 1000 yr at least one impulsive event has occurred from a central source, at or within a few arcseconds of I. Expelled material is now interacting strongly with the surrounding medium. The $2 \mu\text{m}$ continuum image also reveals several dozen stars (including four sets of close binaries), detailed knotty and diffuse reflection nebulae, a shell around a star, and a crescent-shaped feature. We plan to present a more detailed study of the NICMOS data in future work, including a photometric census of the stellar population, the extension of BN’s core, and further H_2 line profile analysis.

We would like to thank Mark McCaughrean for providing ground-based K -band data for stars in OMC-1 and Zolt Levay for assistance with the figures.

REFERENCES

- Allen, D. A. & Burton, M. G. 1993, *Nature*, 363, 54 (AB)
 Axon, D. J., & Taylor, K. 1984, *MNRAS*, 207, 241
 Beckwith, S., Persson, S. E., Neugebauer, G., & Becklin, E. E. 1978, *ApJ*, 223, 464
 Brand, P. W. J. L. 1995, *Ap&SS*, 233, 27
 Burton, M. G. 1992, *Australian J. Phys.*, 45, 463
 Chrysostomou, A., Burton, M. G., Axon, D. J., Brand, P. W. J. L., Hough, J. H., Bland-Hawthorn, J., & Geballe, T. R. 1997, *MNRAS*, 289, 605 (CBA)
 Chrysostomou, A., Hough, J. H., Burton, M. G., & Tamura, M. 1994, *MNRAS*, 268, 325
 Dougados, C., Léna, P., Ridgway, S. T., Christou, J. C., & Probst, R. G. 1993, *ApJ*, 406, 112
 Elitzur, M., Hollenbach, D. J., & McKee, C. F. 1989, *ApJ*, 346, 983
 Gautier, T. N., III, Fink, U., Treffers, R. R., & Larson, H. P. 1976, *ApJ*, 207, L129
 Genzel, R. 1992, in *The Galactic Interstellar Medium*, ed. D. Pfenniger & P. Bartholdi (Berlin: Springer), 373
 Genzel, R., Reid, M. J., Moran, J. M., & Downes, D. 1981, *ApJ*, 244, 884
 Genzel, R., & Stutzki, J. 1989, *ARA&A*, 27, 41
 Gezari, D. Y. 1992, *ApJ*, 396, L43
 Ghez, A. M., McCarthy, D. W., Patience, J. L., & Beck, T. L. 1997, *ApJ*, 481, 378
 Hartigan, P., Raymond, J., & Hartmann, L. 1987, *ApJ*, 316, 323
 Hough, J. H., Chrysostomou, A., Messinger, D. W., Whittet, D. C. B., Aitken, D. K., & Roche, P. F. 1996, *ApJ*, 461, 902
 Kaufman, M. J., & Neufeld, D. A. 1996, *ApJ*, 456, 250
 Lonsdale, C. J., Becklin, E. E., Lee, T. J., & Stewart, J. M. 1982, *AJ*, 87, 1819
 McCaughrean, M. J., & MacLow, M.-M. 1997, *AJ*, 113, 391
 Menten, K. M., & Reid, M. J. 1995, *ApJ*, 445, L157 (MR)

- Minchin, N. R., Hough, J. H., McCall, A., Burton, M. G., McCaughrean, M. J., Aspin, C., Bailey, J. A., Axon, D. J., & Sato, S. 1991, MNRAS, 248, 715
- Nadeau, D., & Geballe, T. R. 1979, ApJ, 230, L169
- O'Dell, C. R., Hartigan, P., Lane, W. M., Wong, S. K., Burton, M. G., Raymond, J., & Axon, D. J. 1997, AJ, 114, 730
- Plambeck, R. L., Wright, M. C. H., Mundy, L. G., & Looney, L. W. 1995, ApJ, 455, L189
- Prosser, C. F., Stauffer, J. R., Hartmann, L., Soderblom, D. R., Jones, B. F., Werner, M. W., & McCaughrean, M. J. 1994, ApJ, 421, 517
- Scoville, N., Kleinmann, S. G., Hall, D. N. B. & Ridgway, S. T. 1983, ApJ, 253, 201
- Smith, M. D., Brand, P. W. J. L., & Moorhouse, A. 1991, MNRAS, 248, 730
- Stone, J. M., Xu, J., & Mundy, L. G. 1995, Nature, 377, 315
- Tedds, J. A., Brand, P. W. J. L., Burton, M. G., Chrysostomou, A., & Fernandes, A. J. L. 1995, Ap&SS, 233, 39
- Thompson, R. I., Rieke, M. J., Schneider, G., Hines, D., & Corbin, M. R. 1997, ApJ, 492, L95
- Wright, M., Sandell, G., Wilner, D. L., & Plambeck, R. L. 1992, ApJ, 393, 225

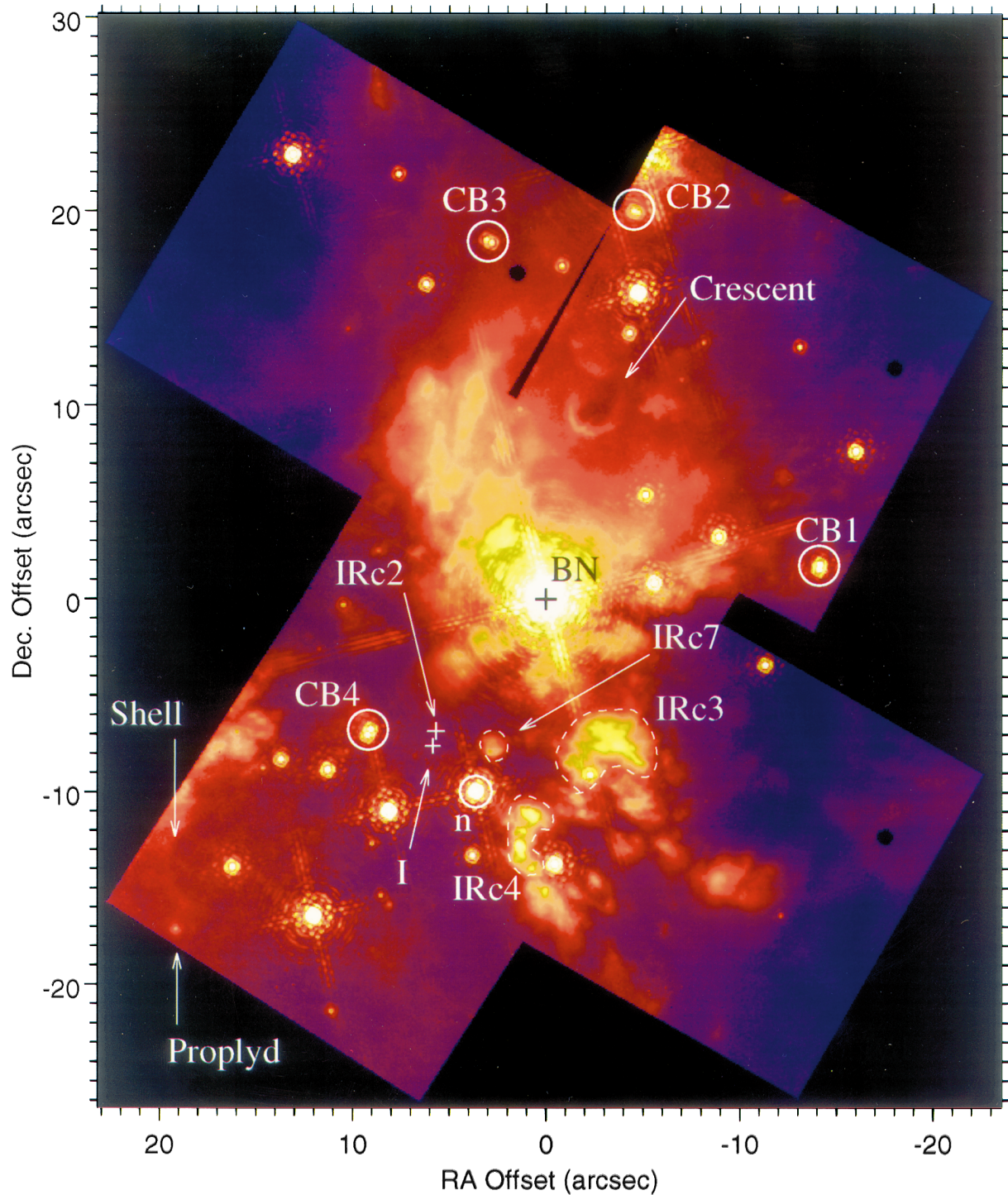


FIG. 1.—Continuum mosaic of the core of OMC-1 at $2.15\ \mu\text{m}$, with objects discussed in the text labeled for reference. The coordinates are relative to BN, as in Figs. 2 and 3. We adopt the J2000 position of BN to be that of radio continuum source B given in Menten & Reid (1995), with R.A. = $5^{\text{h}}35^{\text{m}}14^{\text{s}}.117 \pm 0^{\text{s}}.002$, decl. = $-5^{\circ}22'22''.90 \pm 0''.03$. The $8.7\ \mu\text{m}$ position of IRc2 (Gezari 1992) and the position of radio source I are denoted by white plus signs. IRc3, IRc4, and IRc7 are the extended structures enclosed by dashed lines. The black circular regions denote the locations of the coronagraphic hole. The color scale is logarithmic and ranges from 0.01 ($\sim 14\ \sigma$) for the darkest blue to 0.63 for the onset of white in units of mJy pixel^{-1} (1 pixel = $0''.07577$, FWHM = $0''.18$). The white region extends to the maximum value of $290\ \text{mJy pixel}^{-1}$ at BN. The stellar sources visible in this stretch have fluxes ranging from $m_K \approx 5.4$ (BN) to 16.5.

STOLOVY et al. (see 492, L152)

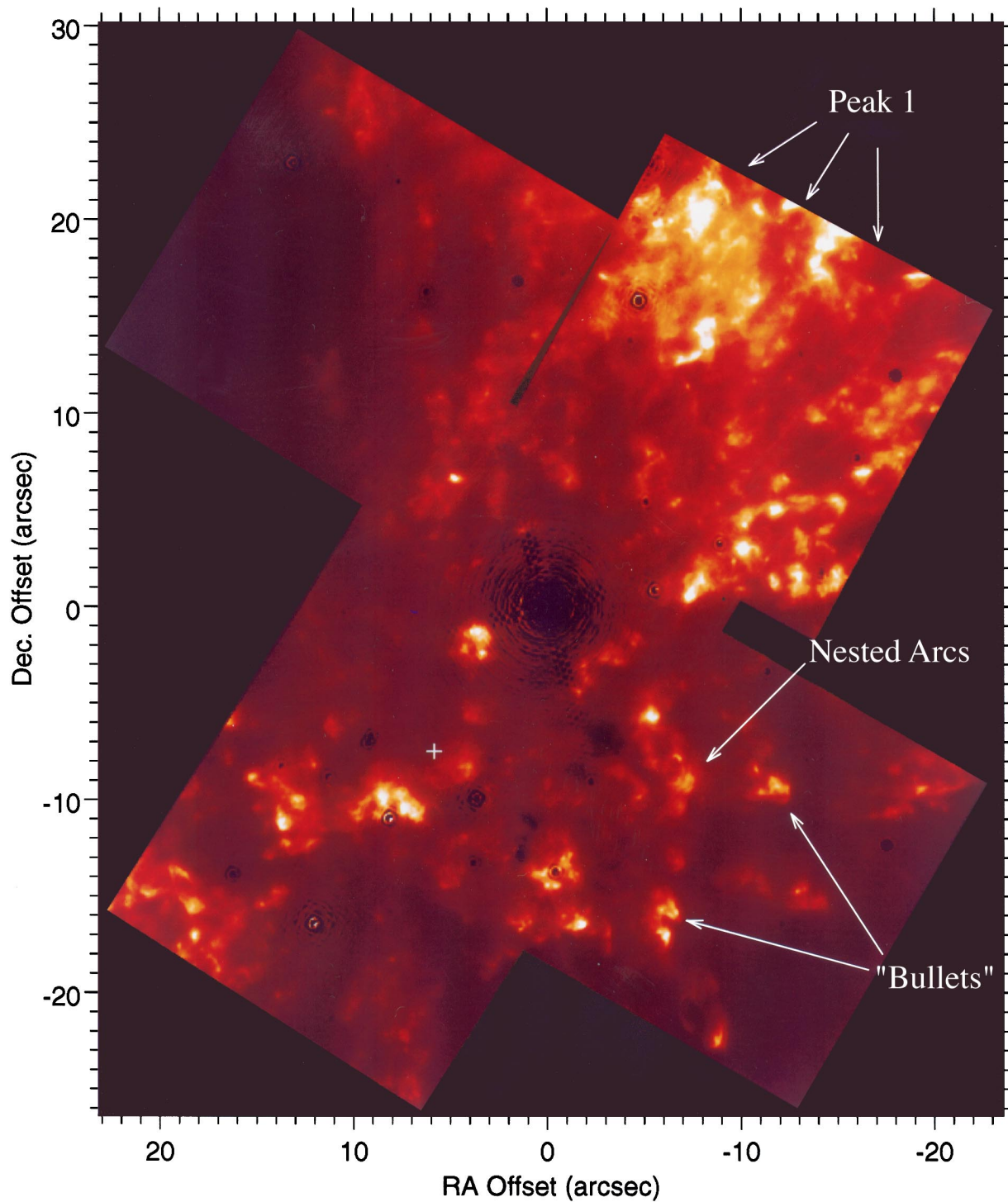


FIG. 2.—Molecular hydrogen mosaic of the core of OMC-1 in the $2.12\ \mu\text{m}$ line. The color scale is linear, increasing from dark to light. The Peak 1 region is indicated in the northwestern part of the image, as are several bullets and the nested arcs to the southwest. A white plus sign denotes the location of suspected outflow source I.

STOLOVY et al. (see 492, L152)

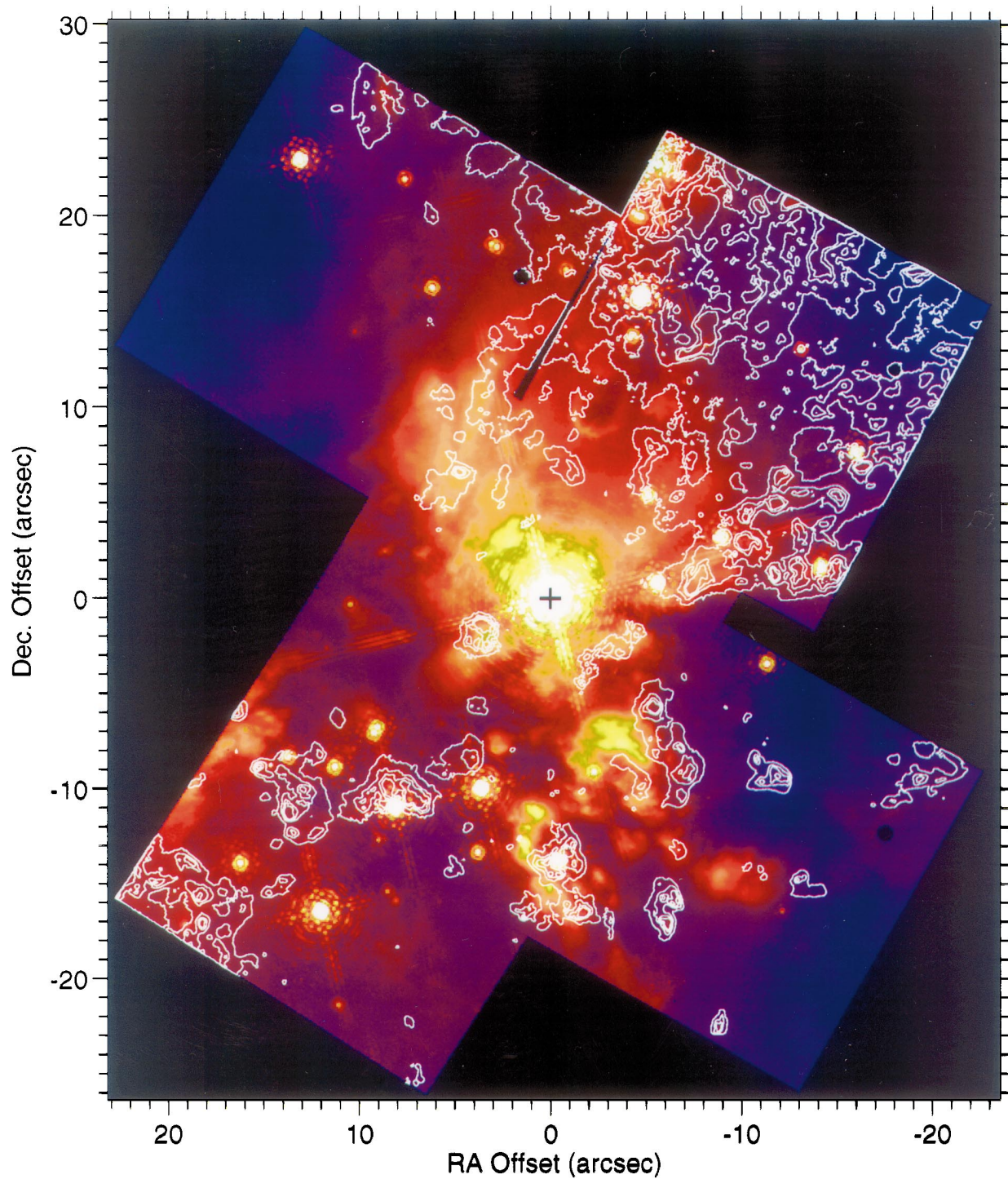


FIG. 3.—Continuum mosaic from Fig. 1 overlaid with white H₂ contours. The contours emphasize strong H₂ emission and range from 4.8 to 15×10^{-16} ergs $\text{s}^{-1} \text{cm}^{-2} \text{pixel}^{-1}$ in linear increments of 3.5×10^{-16} ergs $\text{s}^{-1} \text{cm}^{-2} \text{pixel}^{-1}$.

STOLOVY et al. (see 492, L152)

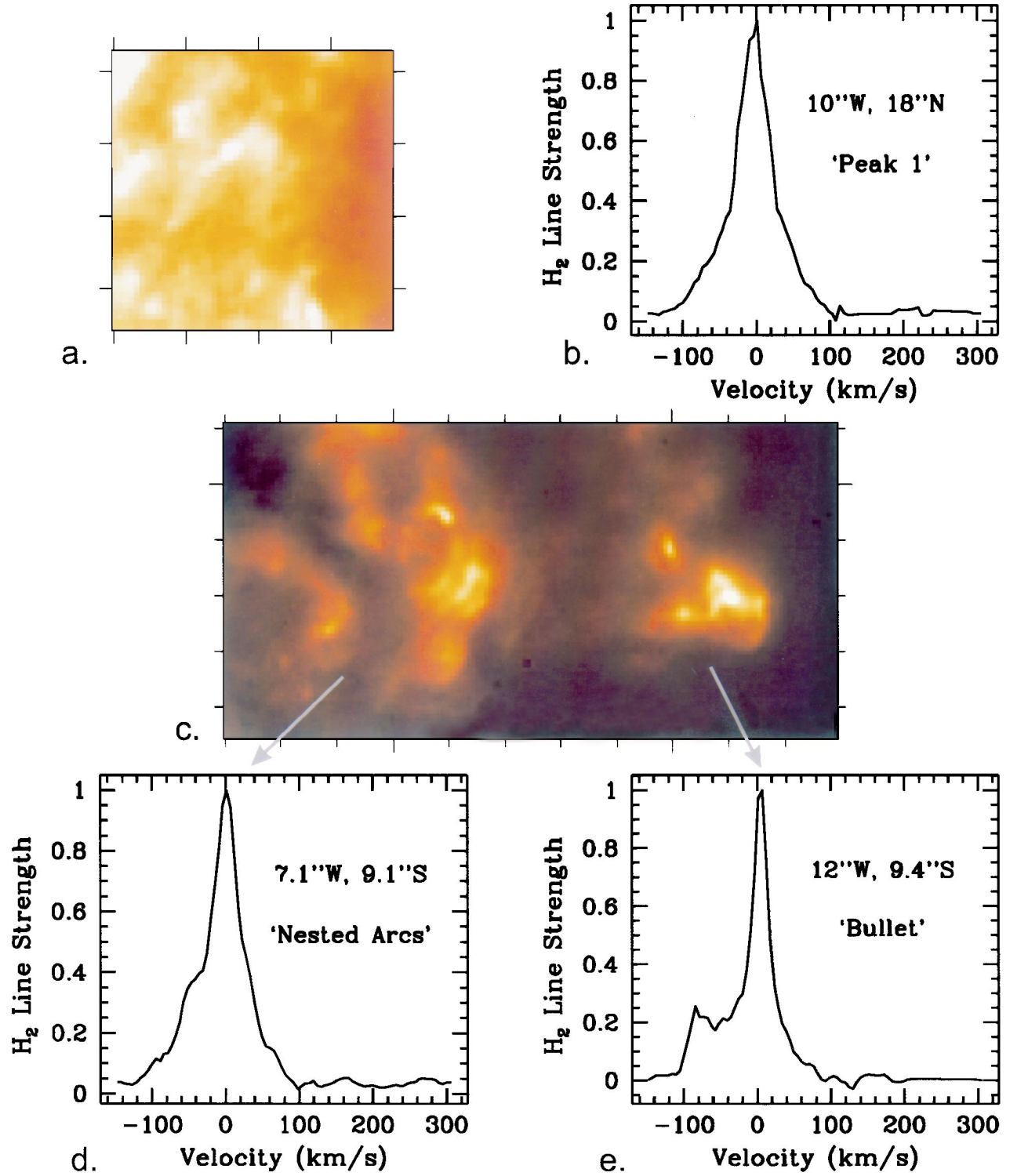


FIG. 4.—Selected H₂ features from Fig. 2 with corresponding line profiles extracted from individual 0''.61 pixels from Fabry-Perot observations of CBA. The short tick marks are spaced by 1''. The position of the center of each image relative to BN is listed in line profile plots, which have $\sim 1''.5$ spatial resolution. (a) $3''.9 \times 3''.9$ region showing diffuse morphology from the Peak 1 region; (b) line profile for (a); (c) $10''.9 \times 5''.6$ region showing nested arcs to the east and bullet to the west; (d) profile for nested arcs; (e) profile for bullet.

STOLOVY et al. (see 492, L153)

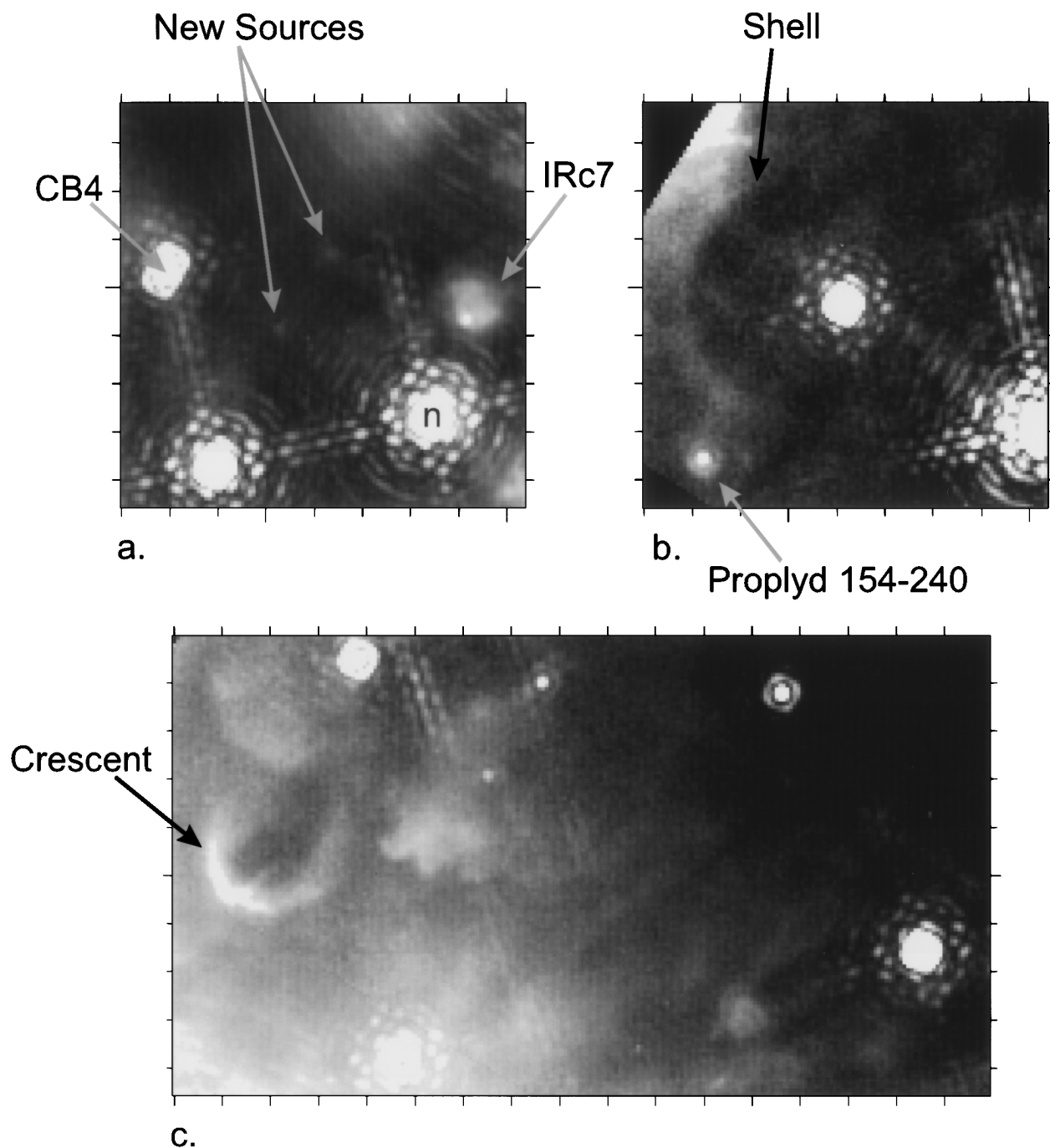


FIG. 5.—Selected continuum features in gray scale (increasing in brightness from black to white), with short tick marks spaced by $1''$. All images have the same magnification factor and have north up and east to the left. (a) $8''.4 \times 8''.4$ region centered on radio source I, located $5''.89$ E and $7''.64$ S of BN. Two new $2\ \mu\text{m}$ faint sources are seen near the center of the image; the northern one is coincident with IRc2-B. Other objects in the field are n (brightest star to the SW), IRc7 (with the fanlike feature extending to the north), and CB4 (binary to the NE). The gray scale ranges from 0.028 (black) to 0.112 (white) mJy pixel^{-1} ; (b) $8''.4 \times 8''.4$ region displaying the shell feature centered on the star located $16''.2$ E and $13''.9$ S of BN. The object in the southwest corner is proplyd 154-240. The gray scale ranges from 0.035 to 0.063 mJy pixel^{-1} ; (c) $17''.0 \times 9''.6$ region displaying the Crescent (left) and downstream features to its north and west. The apex (southern edge) of the Crescent is located $\sim 1''.9$ W, $8''.8$ N of BN. A distinct feature located $\sim 12''.4$ W, $6''.3$ N of BN (bottom right) appears to have a shadow and faint wake. The gray scale ranges from 0.028 to 0.066 mJy pixel^{-1} .

STOLOVY et al. (see 492, L154)